Chang *et al. Energy Mater.* **2025**, *5*, 500117
DOI: 10.20517/energymater.2025.05

Energy Materials

Article

Open Access

High performance anion exchange membrane water electrolysis driven by atomic scale synergy of non-precious high entropy catalysts

Chiung-Wen Chang, Yu-Chieh Ting, Fan-Yu Yen, Guan-Ru Li, Kun-Han Lin*, Shih-Yuan Lu*

Department of Chemical Engineering, National Tsing Hua University, Hsinchu 300044, Taiwan.

***Correspondence to:** Dr./Prof. Kun-Han Lin and Dr./Prof. Shih-Yuan Lu, Department of Chemical Engineering, National Tsing Hua University, No. 101, Section 2, Kuang-Fu Road, Hsinchu 300044, Taiwan. E-mail: kunhan.lin@mx.nthu.edu.tw; sylu@mx.nthu.edu.tw

How to cite this article: Chang, C. W.; Ting, Y. C.; Yen, F. Y.; Li, G. R.; Lin, K. H.; Lu, S. Y. High performance anion exchange membrane water electrolysis driven by atomic scale synergy of non-precious high entropy catalysts. *Energy Mater.* **2025**, *5*, 500117. https://dx.doi.org/10.20517/energymater.2025.05

Received: 8 Jan 2025 **First Decision:** 27 Mar 2025 **Revised:** 16 Apr 2025 **Accepted:** 16 May 2025 **Published:** 9 Jun 2025

Academic Editors: Soo Young Kim, Jiazhao Wang **Copy Editor:** Ping Zhang **Production Editor:** Ping Zhang

Abstract

Anion exchange membrane water electrolysis is one of the key technologies for production of green hydrogen, and developments of highly efficient and durable electrode catalysts in alkaline media are critical for its practical applications. Atomic scale synergy of high entropy materials empowers highly efficient water electrolysis catalysts. Here, Fe, Co, Ni, Cu, and Mo-based high entropy electrode catalysts, including high entropy alloys (FCNCuM) for cathodes and high entropy oxides ($FCNCuMO_x$) for anodes, are developed for high-performance Anion exchange membrane water electrolysis. $FCNCuMO_x$ and FCNCuM exhibit outstanding catalytic efficiency toward oxygen evolution reaction (OER) and hydrogen evolution reaction (HER), respectively, achieving ultralow overpotentials of 183 and 294 mV for OER and 38 and 230 mV for HER at 10 and 500 mA cm^{-2}, respectively, in 1 M KOH. The anion exchange membrane water electrolyzer, using $FCNCuMO_x$ and FCNCuM as the anode and cathode catalysts, respectively, achieves an ultrahigh specific activity of 293 mA mg^{-1} and exhibits outstanding durability with decay of only 0.014% after a 100 h operation at 500 mA cm^{-2}. *In-situ* Raman and *in-situ* X-ray absorption studies disclose that atomic scale synergy between Fe, Co, and Ni, the three main active centers, is responsible for the extraordinary OER activity, and density functional theory calculations reveal that atomic scale synergy between Mo and Ni leads to the outstanding HER performance.

Keywords: Anion exchange membrane water electrolysis, high entropy alloy, high entropy oxide, non-precious metal based catalyst, microwave synthesis

INTRODUCTION

Developing renewable, zero-carbon emission energies is one of the keys to achieving the goal of net-zero emissions by 2050. Hydrogen, in this regard, becomes a primary energy source, making production of green hydrogen an essential technology to replace traditional fossil fuel based hydrogen generation processes. Renewable energy-driven water electrolysis for hydrogen production is considered the green hydrogen production technology in demand. Its prevailing however is hindered by two technical challenges. First, high overpotentials, thus high electrical energies, are required to drive water electrolysis, making it insufficiently cost-effective to compete with traditional fossil fuel based processes. Second, traditional alkaline water electrolysis (AWE) for hydrogen production operates in high concentration alkaline electrolytes (e.g., 20-30 wt% KOH) with a diaphragm membrane implemented as the separator. The high corrosiveness of the electrolyte and the inability of the separator to completely prevent gas crossover between the anode and cathode chambers raise concerns about safety and practicality of AWE for hydrogen production[1]. In recent years, the advent of anion exchange membrane water electrolysis (AEMWE) has taken a significant step forward toward commercial mass production of hydrogen. AEMWE uses a solid-state hydroxide ion conducting polymer membrane, instead of a high concentration alkaline solution, as the electrolyte. This not only enhances safety and practicality of water electrolysis, but also effectively isolates the gases produced at the anode and cathode, facilitating effective gas collection. This development significantly boosts the commercial potential of water electrolysis for green hydrogen production.

Developments of highly efficient and durable electrode catalysts in alkaline media are critical to improve the cost-effectiveness and thus competitiveness of AEMWE for hydrogen production. Noble metal based catalysts, for example, Pt/C for hydrogen evolution reaction (HER) at the cathode and IrO_2 or RuO_2 for oxygen evolution reaction (OER) at the anode, although performing well, are not suitable for large scale commercial production of hydrogen because of the extreme scarcity and high costs of the involved noble metals. Non-precious transition metal based electrocatalysts however have been widely demonstrated to exhibit electrocatalytic efficiency comparable to that of the noble metal based ones. For examples, transition metal oxides, such as Co_2CuO_4[2], $NiFeO_x$[3], CoO, and NiO[4], have been demonstrated excellent efficiency toward catalysis of OER, and transition metal alloys, including NiMo and NiCu[3], have shown high promises as catalysts for HER.

Furthermore, catalysts containing multiple metal elements allow mixed cationic sites to interact with different intermediates, further enhancing catalytic efficiency[5]. In this regard, high entropy materials, composed of atomically well mixed five or more metal elements in the composition, have drawn rapidly increasing research attention in recent years in the field of catalysis, because of the extraordinary catalytic properties arising from cocktail effects, lattice distortions, and high entropy effects of the multiple component materials. For the cocktail effect, unexpected synergies, coming from interactions between atomically well mixed constituent metal elements, may lead to unusual catalytic properties. The lattice distortion and high mixing entropy help stabilize the solid solution phase of the material over other possible undesired phases, such as intermetallic compounds and segregated phases, which contributes to the excellent chemical and structural stability of the materials[6]. Moreover, the compositions, kinds and concentrations of constituent elements, of high entropy materials can be adjusted based on targeted applications and the design freedom for catalysts is huge. With elements of high catalytic activities toward OER and HER included, the constructed high entropy materials are likely to function well as the electrode catalysts for AEMWEs. Wang *et al.*[7] developed a high-entropy oxide (HEO) electrocatalyst $(FeCoNiCrMnCu)_3O_4$ for OER, achieving a low overpotential of 241.4 mV at 10 mA cm^{-2}. Yao *et al.*[8] created a nanoporous quaternary CuNiMoFe catalyst, through etching removal of Al from a high entropy alloy (HEA) CuAlNiMoFe, to acquire an excellent HER efficiency of delivering 100 mA cm^{-2} at 183 mV in

alkaline media. In general, HEOs and HEAs are promising catalysts toward OER and HER, respectively, and coupling of HEO based anodes with HEA based cathodes should prove promising for high performance AEMWEs. In this regard, although several HEA and HEO materials have been investigated for catalyses of HER[8,9] and OER[7,10], respectively, the benefits of coupling HEA cathodes with HEO anodes, particularly those of non-previous metal based ones, for AEMWE remain unexplored and warrants in-depth investigation.

A simple and fast microwave synthesis method was developed to prepare Fe, Co, Ni, Cu, and Mo based high entropy materials, FeCoNiCuMo HEO (termed as FCNCuMO$_X$) and FeCoNiCuMo HEA (termed as FCNCuM), to serve as the electrode catalysts for high performance AEMWEs. These high entropy materials were deposited on carbon nanotubes (CNTs) for uniform dispersion and thus full utilization of the catalysts. The high conductivity of CNTs also helps reduce the charge transport resistances involved in the water electrolysis process to further raise the catalytic efficiency[4]. For comparison purposes, corresponding quaternary catalysts were also fabricated to help investigate the roles played by the five constituent elements, Fe, Co, Ni, Cu, and Mo, in catalyses of OER and HER. The experimental findings were supported by *in-situ* Raman and *in-situ* X-ray absorption spectroscopy (XAS) studies for OER and by density functional theory (DFT) calculations for HER. The HEO catalyst, FCNCuMO$_X$@CNT, and HEA catalyst, FCNCuM@CNT, exhibited the highest catalytic efficiency toward OER and HER, respectively, achieving ultralow overpotentials of 183 and 294 mV for OER and 38 and 230 mV for HER at 10 and 500 mA cm^{-2}, respectively. The AEMWE, taking FCNCuMO$_X$@CNT as the anode catalyst and FCNCuM@CNT as the cathode catalyst, achieved an ultrahigh specific activity of 293 mA mg^{-1} and remarkable operation stability with negligible decay of 0.014% after a 100 h operation under a high current density of 500 mA cm^{-2}. Experimental findings, together with *in-situ* Raman and *in-situ* XAS characterizations, reveal that Fe, Co, and Ni are the main active centers for catalysis of OER and the synergy between them leads to the high catalytic efficiency for OER. As for HER, the experimental findings, together with the DFT calculation analyses, show that Mo and Ni are the main active sites for catalysis of HER and the synergy between them guarantees the excellent HER activity in alkaline media, taking consideration of both hydrogen adsorption energies and energy barriers for water dissociation. The strong OH adsorption ability of Mo teams up with the moderate hydrogen adsorption ability of Ni to give a low energy barrier for water dissociation and balanced hydrogen adsorption and desorption for highly efficient HER. The advantages of high entropy materials as catalysts for water electrolysis are successfully demonstrated and further improvements can be realized through rational composition design of high entropy catalysts.

EXPERIMENTAL

Chemicals

Cobalt(II) acetate tetrahydrate (Co(OAc)$_2$·4H$_2$O, 98%), nickel(II) acetate tetrahydrate [Ni(OAc)$_2$·4H$_2$O, 98%], molybdenum(V) chloride ($MoCl_5$, > 99.6%), platinum (20 wt% on carbon black), iridium (IV) oxide, (IrO_2, 99.99%), and Nafion D-521 dispersion (5% w/w in water) were bought from Alfa Aesar. Iron(II) acetate [Fe(OAc)$_2$, 95%] was obtained from Acros Organics. Copper(II) acetate monohydrate [Cu(OAc)$_2$·H$_2$O, 98%] and ethylene glycol [(CH$_2$OH)$_2$, > 99%] were received from Showa Chemical. Potassium hydroxide (KOH, > 85.0%) was acquired from Honeywell. Carboxyl group-modified CNTs (COOH-CNTs, > 99.0%) were purchased from Golden Innovation. Nickel foam (NF, 95 PPI, 1.7 mm in thickness) was from MAY CHUN Co., Ltd, while Fumatech FAA-3-50 membranes were obtained from Fuel Cell Store. Commercial carbon paper (CP, GDL280) and nickel mesh (NM) were supplied by CeTech and Ing-Jing Precise Industrial Corp, respectively.

Syntheses of FeCoNiCuMo based high entropy catalysts

For preparation of $FCNCuMO_X$@CNT, 60 mg of COOH-CNT were ultrasonically dispersed in 10 mL ethylene glycol for 1 h. A 0.5 × 0.5 cm^2 NF was repeatedly soaked and methanol-lamp dried in the suspension until CNT loading reached 3 mg cm^{-2} (CNT@NF). Precursors of Fe, Co, Ni, Cu, and Mo (0.0051 mmol each) were dissolved in 2.55 mL of ethylene glycol and drop-cast onto CNT@NF, followed by drying at 60 °C for 10 h. The sample was microwave-treated (800 W, 10 s, Ar) to yield $FCNCuMO_X$@CNT. To obtain FCNCuM@CNT, $FCNCuMO_X$@CNT@NF was calcined in a tube furnace under 5% H_2/Ar (250 sccm) at 350 °C for 2 h (10 °C min^{-1}). The final loadings of $FCNCuMO_X$ and FCNCuM were ~1.4 and ~1.2 mg cm^{-2}, respectively. For comparison, ten quaternary catalysts (five oxides, five alloys) were synthesized similarly, excluding one element from the precursor mix. Oxides were used as OER catalysts (anode), and alloys for HER (cathode). For AEMWE assembly, $FCNCuMO_X$@CNT and FCNCuM@CNT were loaded on NM and CP, respectively, to minimize contact resistances.

Fabrication of IrO_2 and Pt/C benchmark electrodes

For alkaline electrolysis, 0.35 mg of IrO_2 (or 1.5 mg of Pt/C) was dispersed in 0.5 mL of mixed solvent (0.4 mL of ethanol, 0.1 mL of deionized (DI) water, and 10 μL of 5 wt% Nafion) and sonicated for 1 h to form a uniform ink. The ink was drop-cast on NF (0.5 × 0.5 cm) and dried at 70 °C for 10 h. The IrO_2 and Pt/C loadings were matched to $FCNCuMO_X$ (1.4 mg cm^{-2}) and FCNCuM (1.2 mg cm^{-2}), respectively. For AEMWE, 1.4 mg of IrO_2 was dispersed in 7 mg of Sustainion XB-7 (5% in ethanol), 1 mL of isopropanol, and 1 mL of DI water (or 6 mg of Pt/C in 30 mg of XB-7), then sonicated for 1 h to obtain a uniform suspension. The IrO_2 (or Pt/C) suspension was applied onto a 1 cm x 1 cm NM (or CP) with spray coating to afford the precious metal based anode, IrO_2@NM (or cathode, Pt/C@CP). Similar to the case of the AWE, the mass loading of IrO_2 and Pt/C was controlled to be the same with that of $FCNCuMO_X$ (1.4 mg cm^{-2}) and FCNCuM (1.2 mg cm^{-2}), respectively for fair comparison.

Pre-treatment of anion exchange membranes

The commercial anion exchange membrane (FAA-3-50) was cut into 3 × 3 cm^2 pieces, immersed in 1 M KOH at room temperature for 24 h for activation, and then soaked in deionized water for another 24 h to thoroughly rinse off residual KOH and remove the polyethylene terephthalate (PET) liner.

Material characterizations

Sample morphologies were observed using a scanning electron microscope (SEM, Hitachi SU8010). Crystalline structures were characterized by X-ray diffraction (XRD, D8 ADVANCE Eco) equipped with a Cu Kα source and high-resolution transmission electron microscopy (HRTEM, JEM-ARM200FTH). The valence states of constituent elements were determined by high-resolution X-ray photoelectron spectroscopy (HR-XPS, PHI Quantera SXM). Prior to XPS characterizations, the sample was treated with argon ion beam sputtering etching to reduce the surface oxide layer that inevitably formed for metallic samples under prolonged exposure to ambient atmosphere. Elemental compositions were measured via inductively coupled plasma-optical emission spectrometry (ICP-OES, Thermo iCAP 7000 SERIES). Raman spectra were obtained using a Raman spectrometer (MRID, ProTrusTech Co., Ltd) with a 532 nm excitation laser to detect OER-active intermediates. XAS of Fe, Co, Ni, Cu, and Mo K-edges was conducted in fluorescence mode at beamline TPS 44A1 of the National Synchrotron Radiation Research Center (NSRRC), Taiwan, using a solid-state detector. The Faradaic efficiencies of OER and HER were assessed by comparing gas yields measured via gas chromatography (GC-2014) with theoretical values calculated from the respective current densities.

Electrochemical characterizations

Electrochemical characterizations were conducted on an electrochemical workstation (CH Instrument, CHi 760E) using a three-electrode system in 1 M KOH under room temperature. The exposed geometric surface area of the working electrodes was controlled to be 0.25 cm^2 (0.5 cm × 0.5 cm). Hg/HgO (1.0 M) and a graphite rod were used as the reference and counter electrodes, respectively. All potentials reported were converted to refer to the reversible hydrogen electrode (RHE) according to E (*vs.* RHE) = E (*vs.* Hg/HgO) + 0.059 pH + 0.105 V. Polarization curves were measured at a scan rate of 1 mV s^{-1}, and the resulting current densities were iR-corrected using a resistance of ~2-2.5 Ω.

Electrolyzer measurements

To assemble the AEMWE, the anion exchange membrane (FAA-3-50) was sandwiched between 1 cm × 1 cm anode and cathode to form the membrane electrode assembly (MEA), which was then integrated with spacers, flow channels, bipolar plates, and end plates, and fastened using a digital torque wrench at 1 $N{\cdot}m^{-2}$. A 1 M KOH electrolyte was supplied to the anode at 30 $mL{\cdot}min^{-1}$, with its temperature maintained at 50 °C using a controlled heating chamber. The polarization curves were recorded within an applied potential window of 1.2 to 2.0 V at a scan rate of 1 mV s^{-1}. And electrochemical impedance spectroscopy (EIS) was conducted at 1.8 V (*vs.* Hg/HgO) within a frequency window of 0.01 Hz to 100 kHz.

Computational methods

All calculations were performed using DFT with the Vienna Ab Initio Simulation Package (VASP)[11,12]. The electron-ion interaction was described with the projector-augmented wave (PAW) method[13,14]. The wavefunctions were expanded using the plane wave basis. The Perdew-Burke-Ernzerhof (PBE)[15] exchange-correlation functional was employed to account for electron exchange and correlation energies. An energy cutoff of 560 eV was applied, and the convergence criterion for geometry optimization was set at 0.02 eV/Å. A FeCoNiCuMo HEA model was constructed using a 4-layer 3 × 3 (111) face-centered cubic (FCC) slab, followed by randomly assigning elements to each lattice point according to the atomic composition determined from ICP-OES. The lattice constant was obtained from experimental data and kept constant throughout the calculations. To mitigate errors arising from interactions between periodically repeated slabs, a vacuum layer of 15 Å was introduced. A k-point grid of 8 × 8 × 1 was sampled using the Monkhorst-Pack scheme for each computation. Spin-polarized calculations were performed to account for the magnetic properties of Fe, Co, and Ni. The adsorption energy (E_{ads}) was calculated using the formula $E_{ads} = E_{A/S} - E_S - E_A$, where $E_{A/S}$, E_S, and E_A were the calculated energies of the adsorption system, substrate, and adsorbate in the gas phase, respectively. ΔG_{H^*} and ΔG_{OH^*} were estimated using

$$\Delta G_{H^*} = E_{ads} + 0.24 \text{ (eV)} \quad (1)$$

$$\Delta G_{OH^*} = E_{ads} + 0.29 \text{ (eV)} \quad (2)$$

The correction factors, 0.24 eV and 0.29 eV, are commonly applied and include contributions from both the zero-point energy and the entropy term[16]. Hydrogen adsorption energies were calculated for 10 different FeCoNiCuMo HEA configurations [Supplementary Figure 1], with each configuration having 18 hollow sites exposed, totaling 180 different adsorption sites. The probability of each adsorption site was weighted based on the concentration of each metal element as determined by ICP-OES to obtain the average adsorption energy of the FeCoNiCuMo HEA model. For the corresponding quaternary samples, the probability of the adsorption sites involving the absent element was set to zero, and the probabilities of the adsorption sites involving the four present elements were re-weighted to obtain the average adsorption energy for the quaternary samples. Transition state structures were estimated using the climbing image nudged elastic band method (CI-NEB)[17] with nine images. Nine images were positioned along the

minimum energy path (MEP), and a spring force constant of -5.0 eV/Å^2 was applied between the images to relax them until the maximum force acting on each atom was less than 0.02 eV/Å.

RESULTS AND DISCUSSION

Materials characterizations

The two high entropy catalysts, FCNCuMO$_x$@CNT and FCNCuM@CNT, were prepared with a simple and fast microwave synthesis method as illustrated in Scheme 1. Briefly, carboxyl group-modified CNTs were first deposited onto the skeleton surfaces of the porous substrate (NF, NM, or CP), followed by drop-casting a mixed Fe, Co, Ni, Cu, Mo precursor solution onto the substrate. The precursor loaded substrate was then treated in a microwave oven to form the HEO catalyst, FCNCuMO$_x$@CNT, used as the OER catalyst at the anode. As for the HER catalyst at the cathode, FCNCuM@CNT, it was obtained from thermal reduction of FCNCuMO$_x$@CNT in an atmosphere of 5% H_2/Ar. For comparison purposes, corresponding quaternary catalysts, both oxides and alloys, were also prepared.

Figure 1A shows the XRD pattern of FCNCuMO$_x$@CNT and FCNCuM@CNT. These high entropy materials were deposited on the surfaces of CNTs as nanoparticles, as evident from Figure 1B for FCNCuMOx@CNT and Figure 1C for FCNCuM@CNT. These nanoparticles have a size of around 6 nm [Figure 1D-F]. For the HEO catalyst, FCNCuM@CNT, two sets of diffraction peaks, (111) and (200) of the rock salt oxide located at 2θ of 37.1° and 43.5° and (311) and (440) of the spinel oxide located at 2θ of 34.4° and 60.6°, were observed from Figure 1A. The broad peak centering around 2θ of 35° can be deconvoluted, as shown in Supplementary Figure 2, to determine the contributions from the spinel and rock salt oxides to be at a molar ratio of around 2:1. Evidently, FCNCuMO$_x$@CNT was composed of a mixture of two HEOs, rock salt and spinel. HRTEM was conducted to further support the conclusion. Figure 1G shows the HRTEM image with interlayer distances of 0.245 and 0.206 nm determined, in good agreement with the d-spacing of the (111) and (200) planes of the rock salt oxide, respectively. Spinel oxide was also detected, as evident from Figure 1H, with an interlayer distance of 0.257 nm observed, corresponding well to d-spacing of the (311) planes of the spinel oxide. As for the HEA catalyst, FCNCuM@CNT, characteristic diffraction peaks located at 2θ of 44.6°, 51.9°, and 76° were observed, as evident from Figure 1A, attributable to a single FCC phase of the HEA. Furthermore, interlayer distances of 0.207 and 0.181 nm were determined from the HRTEM image shown in Figure 1I, in good agreement with the d-spacing of the (111) and (200) planes of the FCC phase, respectively. Evidently, the mixed HEOs of FCNCuMO$_x$@CNT were completely reduced to an FCC HEA, FCNCuM@CNT. Note that the pronounced diffraction peaks located at 2θ of 26.1° for both FCNCuMO$_x$@CNT and FCNCuM@CNT [Figure 1A] were contributed by the presence of CNTs. In addition, the metallic elements of both FCNCuMO$_x$@CNT and FCNCuM@CNT are uniformly distributed in the sample as evident from the STEM-EDS elemental mapping presented in Supplementary Figures 3 and 4, respectively. Furthermore, the metallic compositions of the two catalysts were determined with ICP-OES, as summarized in Supplementary Table 1 for examination. Evidently, the atomic percentages of all constituent elements fall within the 5%-35% range, required for formation of high entropy materials.

XPS analysis was performed to examine the surface oxidation states of FCNCuMO$_x$@CNT and FCNCuM@CNT. Figure 2 shows the HR-XPS spectra of Fe 2p, Co 2p, Ni 2p, Cu 2p, and Mo 3d for both catalysts. For FCNCuMO$_x$@CNT, the Fe 2p spectrum [Figure 2A] reveals six peaks attributed to Fe^{2+} ($2p_{3/2}$ 709.1 eV, $2p_{1/2}$ 722.3 eV), Fe^{3+} ($2p_{3/2}$ 712.1 eV, $2p_{1/2}$ 726.0 eV), and satellite peaks ($2p_{3/2}$ 715.8 eV, $2p_{1/2}$ 732.2 eV)[18,19] [Figure 2A]. The Co 2p spectrum [Figure 2B] displays peaks corresponding to Co^{2+} ($2p_{3/2}$ 781.0 eV, $2p_{1/2}$ 797.4 eV), Co^{3+} ($2p_{3/2}$ 779.7 eV, $2p_{1/2}$ 796.3 eV), and satellite peaks ($2p_{3/2}$ 784.6 eV, $2p_{1/2}$ 802.5 eV)[20,21]. Similarly, the Ni 2p spectrum [Figure 2C] shows features for Ni^{2+} ($2p_{3/2}$ 854.0 eV, $2p_{1/2}$ 872.0 eV), Ni^{3+} ($2p_{3/2}$ 856.0 eV, $2p_{1/2}$ 873.5 eV), and satellite peaks ($2p_{3/2}$ 861.5 eV, $2p_{1/2}$ 879.5 eV)[22]. The

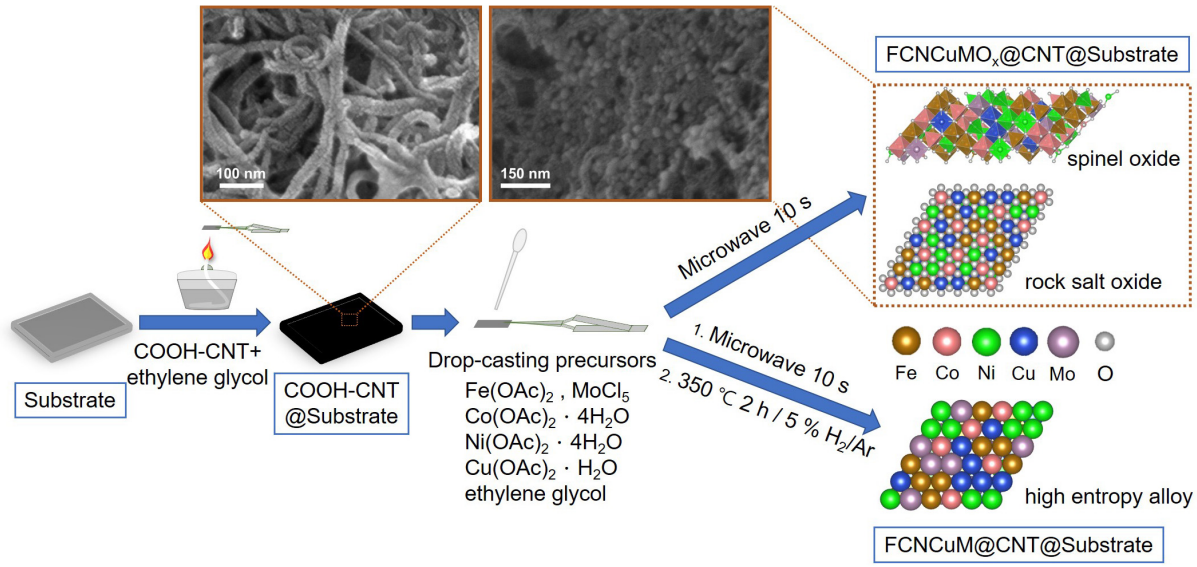

Scheme 1. Schematic illustration for preparation of FCNCuMO$_X$@CNT and FCNCuM@CNT. CNTs: Carbon nanotubes.

Cu 2p peaks [Figure 2D] include Cu^{2+} ($2p_{3/2}$ 933.3 eV, $2p_{1/2}$ 952.9 eV) and satellite peaks ($2p_{3/2}$ 941.4 eV, $2p_{1/2}$ 960.7 eV)[23]. Finally, the Mo 3d spectrum [Figure 2E] consists of two peaks corresponding to Mo^{6+} ($3d_{5/2}$ 232.1 eV, $3d_{3/2}$ 235.2 eV)[24].

As for FCNCuM@CNT, metallic states of the five constituent elements, absent from the HR-XPS spectra of FCNCuMO$_X$@CNT, are detected in addition to the oxidized states. The Fe 2p spectrum [Figure 2A] consists of eight peaks, assigned to Fe^0 ($2p_{3/2}$ 707.0 eV, $2p_{1/2}$ 720.0 eV), Fe^{2+} ($2p_{3/2}$ 709.4 eV, $2p_{1/2}$ 722.5 eV), Fe^{3+} ($2p_{3/2}$ 712.0 eV, $2p_{1/2}$ 725.0 eV), and satellite peaks ($2p_{3/2}$ 714.9 eV, $2p_{1/2}$ 730.6 eV)[25,26]. The Co 2p spectrum [Figure 2B] is composed of six constituent peaks, corresponding to Co^0 ($2p_{3/2}$ 778.0 eV, $2p_{1/2}$ 793.0 eV), Co^{2+} ($2p_{3/2}$ 781.1 eV, $2p_{1/2}$ 796.2 eV), and satellite peaks ($2p_{3/2}$ 786.2 eV, $2p_{1/2}$ 803.0 eV)[20,21]. The Ni 2p spectrum [Figure 2C] features eight peaks, assigned to Ni^0 ($2p_{3/2}$ 852.8 eV, $2p_{1/2}$ 870.0 eV), Ni^{2+} ($2p_{3/2}$ 854.0 eV, $2p_{1/2}$ 872.0 eV), Ni^{3+} ($2p_{3/2}$ 856.0 eV, $2p_{1/2}$ 873.5 eV), and satellite peaks ($2p_{3/2}$ 858.2 eV, $2p_{1/2}$ 876.9 eV)[22,27]. The Cu 2p spectrum [Figure 2D] shows four peaks corresponding to Cu^0 ($2p_{3/2}$ 932.7 eV, $2p_{1/2}$ 952.5 eV) and Cu^{2+} ($2p_{3/2}$ 934.8 eV, $2p_{1/2}$ 954.7 eV)[23,28]. Lastly, the Mo 3d spectrum [Figure 2E] contains six peaks, attributed to Mo^0 ($3d_{5/2}$ 228.1 eV, $3d_{3/2}$ 231.0 eV), Mo^{4+} ($3d_{5/2}$ 229.2 eV, $3d_{3/2}$ 232.9 eV), and Mo^{6+} ($3d_{5/2}$ 232.0 eV, $3d_{3/2}$ 235.2 eV)[24,29]. Note that the oxidized states of FCNCuM@CNT come from the surface oxidation that occurs when the sample is exposed to ambient atmosphere before XPS characterizations. The impact of surface oxidation is particularly intense for the present samples because of the small size of the catalyst nanoparticles, around only 6 nm. The surface oxidation states of the quaternary samples were also examined with XPS characterizations for comparison. Supplementary Figures 5-9 show the HR-XPS spectra of Fe 2p, Co 2p, Ni 2p, Cu 2p, and Mo 3d for all ten quaternary catalysts. Similar to the quinary samples, metallic states of all constituent elements are detected in CNCuM@CNT [Supplementary Figure 5], FNCuM@CNT [Supplementary Figure 6], FCCuM@CNT [Supplementary Figure 7], FCNM@CNT [Supplementary Figure 8], and FCNCu@CNT [Supplementary Figure 9], but not in CNCuMO$_X$@CNT [Supplementary Figure 5], FNCuMO$_X$@CNT [Supplementary Figure 6], FCCuMO$_X$@CNT [Supplementary Figure 7], FCNMO$_X$@CNT [Supplementary Figure 8], and FCNCuO$_X$@CNT [Supplementary Figure 9]. Moreover, the deconvolution results of the five constituent elements in these ten quaternary samples are nearly identical to those in the quinary samples [Supplementary Notes 1-5], indicating that the surface oxidation states of the quaternary samples are similar to those of the quinary

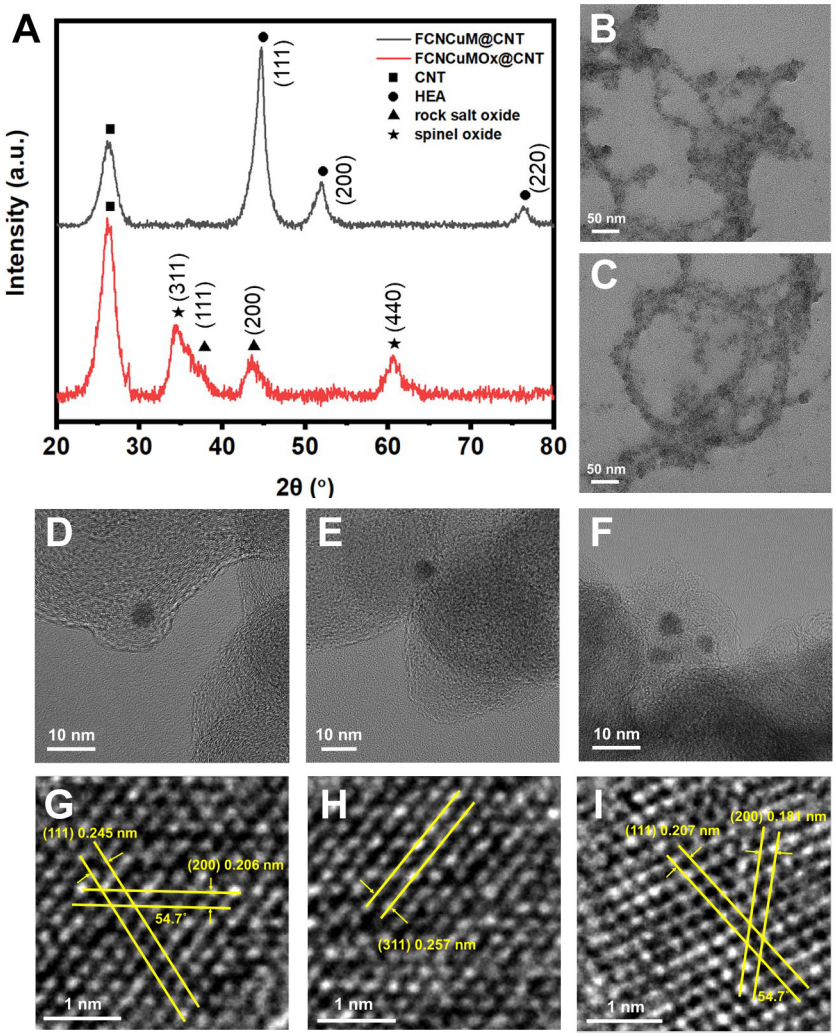

Figure 1. (A) XRD patterns of FCNCuMO$_X$@CNT and FCNCuM@CNT. TEM images (B, D and E) and HRTEM images (G and H) of FCNCuMO$_X$@CNT. TEM images (C and F) and HRTEM images of (I) FCNCuM@CNT. XRD: X-ray diffraction; CNTs: carbon nanotubes; HRTEM: high-resolution transmission electron microscopy; TEM: transmission electron microscopy.

samples.

XAS was conducted to gain further insights on the characteristics of the oxidation states of the constituent elements of the two samples. Different from XPS, a surface sensitive characterization, XAS offers information on the average oxidation states of the bulk of the samples. Supplementary Figure 10 shows the X-ray absorption near edge structure (XANES) spectra of FCNCuMO$_X$@CNT and FCNCuM@CNT. Evidently, the absorption edge positions, thus the valence states, of the constituent elements of FCNCuM@CNT downshift to lower absorption energies as compared to those of the corresponding elements of FCNCuMO$_X$@CNT. The absorption edge positions of the constituent elements of FCNCuM@CNT however are still significantly higher than those of the corresponding metal foils, again attributable to the great impact of surface oxidation on the average oxidation states of the ultra-small size nanoparticles. In conclusion, the outcome of XAS is consistent with that of HR-XPS.

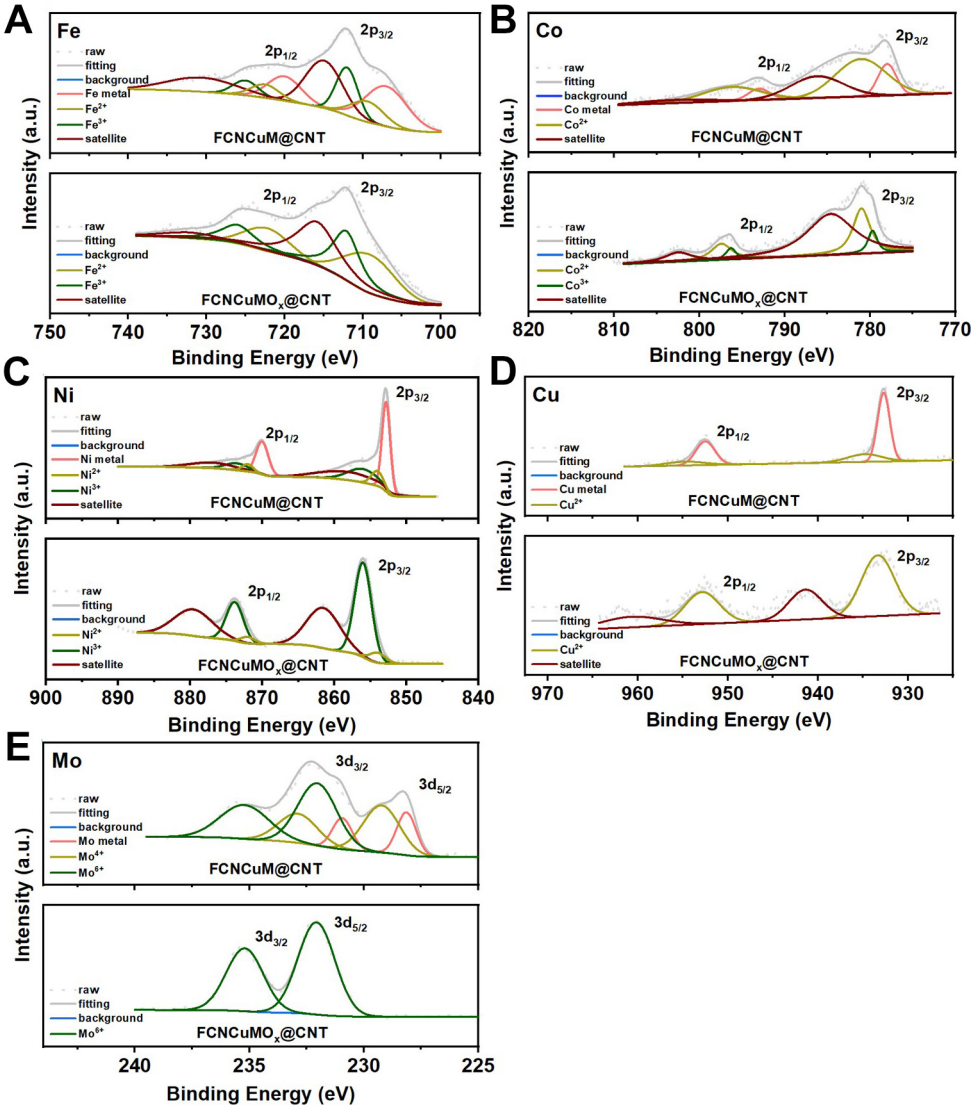

Figure 2. HR-XPS spectra of (A) Fe 2p, (B) Co 2p, (C) Ni 2p, (D) Cu 2p, and (E) Mo 3d of FCNCuMOX@CNT and FCNCuM@CNT. HR-XPS: High-resolution X-ray photoelectron spectroscopy; CNTs: carbon nanotubes.

Electrochemical characterizations

Electrochemical performances of the two high entropy (quinary) and ten quaternary samples, along with the two benchmark catalysts, Pt/C for HER and IrO_2 for OER, were investigated in 1 M KOH for AWE. Here, FCNCuMO$_X$@CNT, CNCuMO$_X$@CNT, FNCuMO$_X$@CNT, FCCuMO$_X$@CNT, FCNMO$_X$@CNT, FCNCuO$_X$@CNT, and commercial IrO_2 were used as the OER catalysts. Supplementary Figure 11 shows the OER linear sweep voltammetry (LSV) polarization curves and corresponding Tafel plots of the seven samples for comparison. Four points can be observed. First, all multi-element oxide samples exhibit better OER catalytic performances than the benchmark catalyst, IrO_2 (η_{10} = 245 mV, η_{500} = 486 mV), indicating the advantage of synergetic interactions realized in the multi-element oxides. Second, all quaternary samples exhibit similar electrochemical performances, including FNCuMO$_X$@CNT (η_{10} = 212 mV, η_{500} = 343 mV, Tafel slope = 49.5 mV dec^{-1}), FCCuMO$_X$@CNT (194 mV, 352 mV, 53.3 mV dec^{-1}), FCNMO$_X$@CNT (185 mV, 320 mV, 51.5 mV dec^{-1}), FCNCuO$_X$@CNT (190 mV, 318 mV, 69.2 mV dec^{-1}), except for CNCuMO$_X$@CNT (227 mV, 383 mV, 77.2 mV dec^{-1}). Evidently, the presence of Fe is critical on catalysis of

OER. Third, the quinary sample of high configurational entropy, FCNCuMO$_X$@CNT, exhibits the highest OER activity (η_{10} = 183 mV, η_{500} = 294 mV), demonstrating the stronger cocktail effect of the five-element oxides over those of the four-element oxides. Fourth, the catalysts with co-existence of Fe, Co, and Ni, including FCNCuMO$_X$@CNT, FCNCuO$_X$@CNT, and FCNMO$_X$@CNT, show higher catalytic efficiency than those without the co-existence of Fe, Co, and Ni, implying that the synergy between Fe, Co, and Ni promotes catalysis of OER.

To investigate the mechanism of OER catalyzed by FCNCuMO$_X$@CNT, *in-situ* Raman spectroscopy was conducted. Supplementary Figure 12 shows the *in-situ* Raman spectra of FCNCuMO$_X$@CNT in 1 M KOH recorded at increasing applied potentials. Evidently, a multi-peak broad feature band appears within the wavenumber range of 460-720 cm^{-1} at open circuit potential (OCP). This broadband can be attributed to one Raman active mode (A_{1g}, ~550 cm^{-1}) of the rock salt structure[30] and two Raman active modes (T_{2g}, ~507 cm^{-1} and A_{1g}, ~670 cm^{-1}) of the spinel structure[31]. The contribution of the spinel structure can be further divided into two sub-peaks, one located in the wavenumber range of 460 cm^{-1} to 660 cm^{-1} for the octahedral group and the other located between 660 and 720 cm^{-1} for the tetrahedral group of the spinel oxide[32]. The combined showing of the feature modes of both rock salt and spinel structures is in good agreement with the finding that FCNCuMO$_X$@CNT contains both spinel oxide and rock salt oxide [Figure 1A]. Upon raising the applied potential to 1.416 V, the two feature Raman bands centering at 480 and 556 cm^{-1} become more pronounced, with enhanced peak intensity by 1.11 and 1.17 folds, respectively, as compared to those at OCP. This phenomenon signifies emergence of OER-active intermediates, NiOOH and FeOOH. Additionally, at an applied potential of 1.456 V, the intensity of the feature Raman band centering at 508 cm^{-1} increases by 1.42 times as compared to that at OCP, attributable to the emergence of another OER-active intermediate, CoOOH[33]. Emergence of the OER-active intermediates, including NiOOH, CoOOH, and FeOOH, indicates further oxidation of Ni, Co, and Fe on the surface of FCNCuMO$_X$@CNT under elevated anodic potentials to trigger the OER. Consequently, Ni, Co, and Fe serve as the active sites of FCNCuMO$_X$@CNT for catalysis of OER. Fe is particularly important in this regard, as it significantly impacts the OER activity of NiOOH. Lin *et al.*[34] found that Fe-doping alters the rate determining step (RDS) of the OER on NiOOH, greatly decreasing the Tafel slope of NiOOH. In addition, Fe-doping also reduces the kinetic energy barrier of the RDS. Our experimental results are in line with the above finding. For the case of CNCuMO$_X$@CNT, without the presence of Fe and thus lack of generation of FeOOH and the enhancing effect toward the OER activity of NiOOH, its OER activity is the lowest among all multi-element oxide catalysts.

To examine the roles played by the five constituent elements of FCNCuM@CNT toward catalysis of HER, the six multi-element alloy catalysts samples, including FCNCuM@CNT, CNCuM@CNT, FNCuM@CNT, FCCuM@CNT, FCNM@CNT, FCNCu@CNT, together with commercial Pt/C, were characterized for catalytic performances toward HER. Supplementary Figure 13 shows the HER LSV polarization curves and Tafel plots of the samples, respectively. Several points can be made. First, the overpotentials achieved by FCNCu@CNT and FCCuM@CNT (η_{10} = 68, 57 mV > 50 mV; η_{500} = 320, 303 mV > 300 mV), without the simultaneous presence of Ni and Mo, are appreciably higher than those of the other four multi-element alloy catalysts, implying the active roles played by Ni and Mo toward catalysis of HER[35]. The synergy between them effectively promotes catalysis of HER. Second, among all quaternary alloy catalysts, FCNM@CNT shows the best performance (η_{10} = 43 mV; η_{500} = 228 mV), as outstanding as the HEA catalyst, FCNCuM@CNT (η_{10} = 38 mV < 50 mV; η_{500} = 230 mV < 250 mV), implying the relative inertness of Cu toward catalysis of HER. Third, the mechanism of HER involves three fundamental steps, including Volmer step (electrochemical hydrogen adsorption), Heyrovsky step (electrochemical hydrogen desorption), and Tafel step (chemical hydrogen desorption). When treating the Volmer, Heyrovsky, and Tafel step as the

RDS, the theoretical Tafel slopes are derived to be 120, 40, and 30 mV dec^{-1}, respectively. From Supplementary Figure 13B, the Tafel slope of FCNCuM@CNT is 104 mV dec^{-1}, falling between 120 and 40 mV dec^{-1}, indicating that the Volmer and Heyrovsky steps are comparable[36]. Fourth, FCNCuM@CNT exhibits the highest HER activity among all multi-element alloy catalysts, again demonstrating the stronger cocktail effect of the five-element alloy over those of the four-element alloys. The HER catalytic performances of FCNCuM@CNT, although not as good as Pt/C (η_{10} = 12 mV, η_{500} = 174 mV), are considered outstanding for non-precious metal based HER catalysts. Figure 3A and B summarizes η_{10}, η_{500}, and Tafel slopes of all sample catalysts toward OER and HER, respectively. Evidently, FCNCuMO_X@CNT and FCNCuM@CNT exhibit outstanding catalytic performances toward OER and HER, respectively, making them promising catalysts for anode and cathode, respectively, of AEMWEs. The coupling of FCNCuMO_X@CNT and FCNCuM@CNT is expected to outperform the IrO_2//Pt/C couple for AEMWEs since the combined overpotentials for OER and HER of AWE of the FCNCuMO_X@CNT//FCNCuM@CNT couple, 221 mV for 10 mA cm^{-2} and 524 mV for 500 mA cm^{-2}, are appreciably lower than those of the IrO_2//Pt/C couple, 257 mV for 10 mA cm^{-2} and 660 mV for 500 mA cm^{-2}.

Furthermore, Faradaic efficiency of FCNCuMO_X@CNT and FCNCuM@CNT for OER and HER was determined at current densities of 100 and -100 mA cm^{-2}, respectively, for a duration of 60 min. As shown in Supplementary Figure 14, the measured quantities of O_2 and H_2 generated in the experiment closely match the theoretical values calculated based on the respective current densities, giving Faradaic efficiency close to 100% and confirming the absence of side reactions during OER and HER.

In-situ XAS

In-situ XAS was conducted to gain deeper mechanistic insights on the OER catalyzed by FCNCuMO_X@CNT. Figure 4A-E shows the XANES spectra at K-edge of Fe, Co, Ni, Cu, and Mo during OER, with the applied potentials increasing from OCP to 0.65 V (*vs.* Hg/HgO) and back to OCP in 1 M KOH. The absorption edges of Co and Ni upshift to higher energies upon raising the applied potential from OCP to 0.65 V and downshift back to lower energies when the applied potential returns to OCP, implying further oxidation of Co and Ni to higher valence states under anodic potentials for formation of active species of higher valences for catalysis of OER. On the contrary, the absorption edge of Mo experiences a slight downshift at 0.65 V, implying its relative inertness toward catalysis of OER. Finally, the absorption edges of Fe and Cu remain almost unchanged under variations of the applied potentials, indicating the stable oxidation states of Fe and Cu under anodic potentials. From XANES spectra, one can conclude that Co and Ni are active sites toward catalysis of OER. The roles played by Fe, Cu, and Mo are to be further examined and confirmed with Fourier-transformed extended X-ray absorption fine structure (FT-EXAFS) spectra.

Corresponding FT-EXAFS spectra of Fe, Co, Ni, Cu, and Mo are shown in Figure 4F-J, from which variations in local coordination environments of the metal centers under anodic potentials can be examined for their involvement in catalysis of OER. The analysis is focused on the first shells, the metal-O coordination, of the spectra for data reliability and accuracy. First, the FT-EXAFS spectra of Cu and Mo remain invariant upon variations of the applied potentials, indicating constant local coordination environments of the two elements during OER and thus the inertness of Cu and Mo toward catalysis of OER. On the contrary, the oscillation amplitudes of the FT-EXAFS spectra of Fe and Co increase when raising the applied potential from OCP to 0.65 V (*vs.* Hg/HgO) [Figure 4F and G], indicating enhancements in coordination extent with neighboring species, which can be attributed to the coordination of Fe and Co with OH^- under anodic potentials for catalysis of OER. Note that, for OER in alkaline media, the active site is under continuing attacks of OH^- to generate hydroxides, oxides, and finally oxyhydroxides for release of oxygen and recovery of the active site. One thus concludes that Fe and Co are actively involved in catalysis

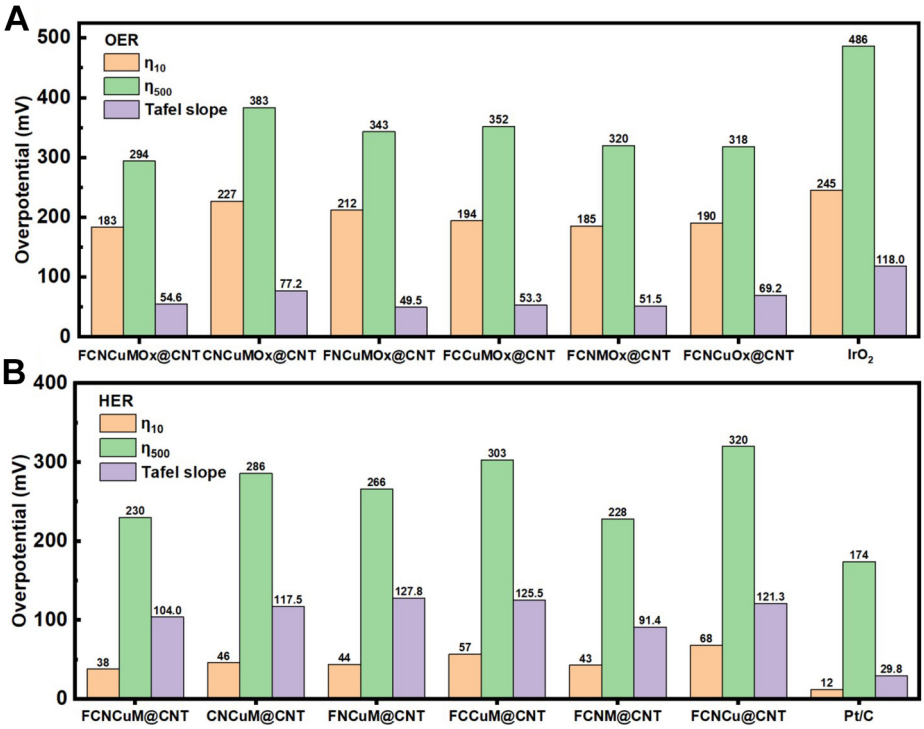

Figure 3. Electrochemical characterizations of $FCNCuMO_X$@CNT, FCNCuM@CNT, and benchmark electrodes, Pt/C and IrO_2, in 1 M KOH. Summary of Tafel slope and overpotentials, η_{10} and η_{500}, for (A) OER and (B) HER achieved by all sample catalysts. CNTs: Carbon nanotubes; OER: oxygen evolution reaction; HER: hydrogen evolution reaction.

of OER[37]. As for the FT-EXAFS spectra of Ni, the situation is more complicated. The oscillation amplitude drops, accompanied by a slight downshift in coordination distances [Figure 4H]. Here, two different motifs can be identified for the Ni-O coordination shell, $Ni\text{-}O_{short}$ and $Ni\text{-}O_{long}$, as shown in Figure 4K. $Ni\text{-}O_{short}$ accounts for nickel of a higher valance state, such as NiOOH, whereas $Ni\text{-}O_{long}$ is contributed by nickel of a lower valence state, such as $Ni(OH)_2$ and NiO. The first shells of the FT- EXAFS spectra of Ni recorded at OCP and 0.65 V can be fitted to reveal the detailed coordination environment of Ni [Figure 4L]. For the case of Ni at OCP, it is purely $Ni\text{-}O_{long}$, whereas for the case of Ni at 0.65 V, it is a combination of 20% $Ni\text{-}O_{long}$ and 80% $Ni\text{-}O_{short}$, as summarized in Supplementary Table 2. Upon raising the applied potential from OCP to 0.65 V, the oscillation amplitude of $Ni\text{-}O_{long}$ decreases while the oscillation amplitude of $Ni\text{-}O_{short}$ emerges and dominates, leading to a slight shrinkage of the average Ni-O bond caused by elevation of the valence state of Ni[38,39]. In conclusion, Ni is also an active site toward catalysis of OER. With the above analyses, it can be concluded that Fe, Co, and Ni are active sites of $FCNCuMO_X$@CNT for catalysis of OER, consistent with the findings observed from *in-situ* Raman study.

AEMWE characterizations

$FCNCuMO_X$@CNT and FCNCuM@CNT perform well as catalysts for OER and HER, respectively, in AWE, and were further applied as the catalysts for anode and cathode, respectively, in AEMWE. For AEMWEs, the contact between the electrodes, anode and cathode, and the anion exchange membrane is critical, concerning the contact resistance of the MEA. In this regard, suitable ubstrates for support of the catalysts are used to minimize the contact resistance to improve the electrochemical performances of the assembled AEMWE. Here, $FCNCuMO_X$@CNT and FCNCuM@CNT were loaded on NM and CP to serve as the anode and cathode, respectively for AEMWEs. For comparison purposes, corresponding quaternary catalysts and noble metal-based AEMWEs were also fabricated for characterizations. The polarization

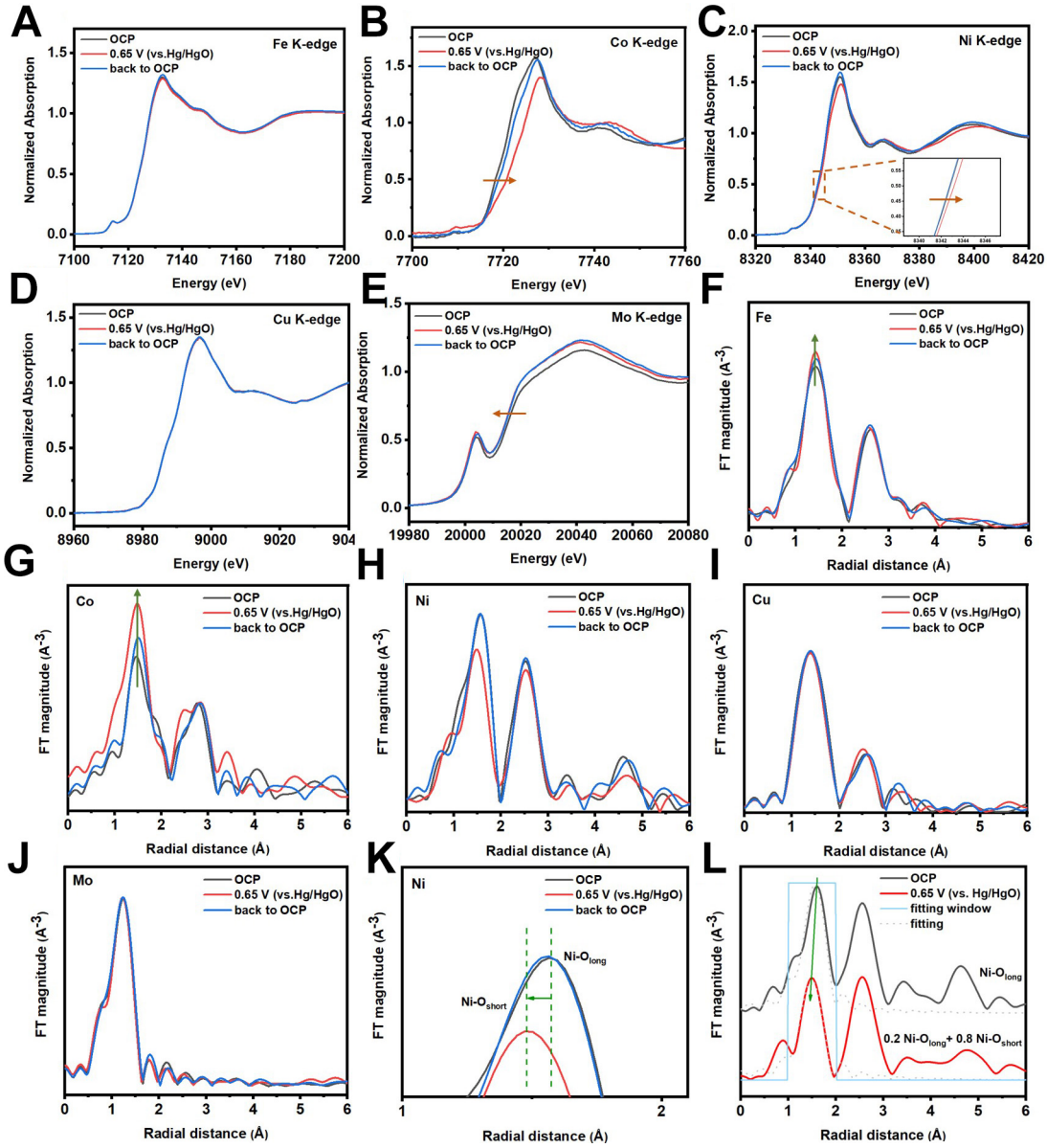

Figure 4. *In-situ* XAS characterizations of FCNCuMO$_X$@CNT under variations of applied potentials. XANES spectra of K-edge of (A) Fe, (B) Co, (C) Ni, (D) Cu, and (E) Mo; Inset figure of panel (C) shows locally enlarged absorption spectra; FT-EXAFS spectra of K-edge of (F) Fe, (G) Co, (H) Ni, (I) Cu, and (J) Mo; (K) Locally enlarged spectra of panel (H); (L) Fitted first-shells of Ni at OCP and 0.65 V. CNTs: Carbon nanotubes; XAS: X-ray absorption spectroscopy; XANES: X-ray absorption near edge structure; FT-EXAFS: fourier-transformed extended X-ray absorption fine structure; OCP: open circuit potential.

curves of the seven AEMWEs are shown in Supplementary Figure 15, with the current densities achieved at 1.8 and 2.0 V displayed in Figure 5A for comparison. In addition, the current densities achieved at 1.8 V ($I_{1.8V}$) from AEMWE measurements are correlated with the sums of η_{10} (η_{10_sum}) determined from AWE measurements as presented in Supplementary Table 3 and the attached figure. Evidently, $I_{1.8V}$ correlates well with η_{10_sum}, with lower η_{10_sum} giving higher $I_{1.8V}$. Several points are further observed from Figure 5A, Supplementary Figure 15, and Supplementary Table 3. First, the quinary catalysts, FCNCuMO$_X$@CNT and FCNCuM@CNT, based AEMWE and AWE achieve the highest current densities and lowest combined overpotentials, confirming again the enhancement induced from the positive synergy of Fe, Co, Ni, Cu, and

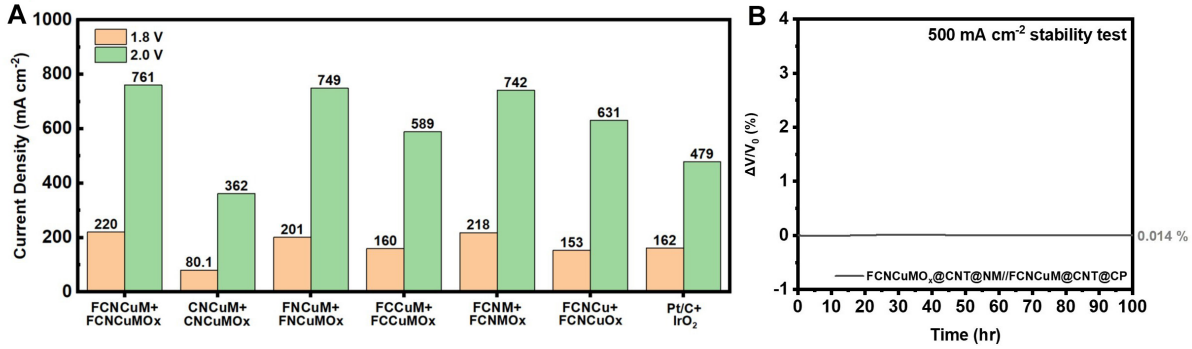

Figure 5. (A) Summary of current densities achieved at 1.8 and 2.0 V by sample AEMWEs; (B) Operation stability of FCNCuMO$_X$@CNT and FCNCuM@CNT based AEMWE under current density of 500 mA cm^{-2} for 100 h. CNTs: Carbon nanotubes; AEMWE: anion exchange membrane water electrolysis.

Mo. Second, the Fe-absent catalysts, CNCuMO$_X$@CNT and CNCuM@CNT, based AEMWE and AWE exhibit the lowest current densities and highest combined overpotentials. This can be explained as follows. The OER occurring at the anode is the bottleneck of the water electrolysis process, because of the high overpotential required to trigger the sluggish four-electron transfer reactions involved. Consequently, the OER activity of the anode catalyst plays a dominant role in determining the electrochemical performance of the AEMWE and AWE. And, as discussed in an early section, Fe is a critical component to OER-activities. The Fe-absent catalysts, CNCuMO$_X$@CNT and CNCuM@CNT, based AEMWE and AWE thus exhibit the worst performance among all characterized samples.

In addition to polarization curves, EIS was conducted to examine the charge transport and charge transfer resistances involved in the six sample AEMWEs. Supplementary Figure 16 shows the Nyquist plots for the six sample AEMWEs recorded at 1.8 V and 50 °C. These Nyquist plots were fitted with an equivalent circuit model (inset of Supplementary Figure 16), composed of five electrical components, including a system resistor (R_0), two charge transfer resistors (R_1 for the cathode and R_2 for the anode), and two constant phase element capacitors (CPE_1 for the cathode and CPE_2 for the anode). The fitting results for R_0, R_1, and R_2 are summarized in Supplementary Table 4 for comparison, from which three key points can be made. First, R_0, obtained as the intercept on the horizontal axis at high frequencies, corresponds to the high frequency resistance (HFR) of the AEMWE and is mainly contributed by the contact resistances between the two electrodes and the ion exchange membrane within the MEA[1]. The R_0 values remain almost constant across the six sample AEMWEs since the same kinds of substrates, NM for the anode and CP for the cathode, were used for assembly of the six sample AEMWEs. Second, the values of R_2, the charge transfer resistance at the anode (OER), are significantly higher than those of corresponding R_1, the charge transfer resistance at the cathode (HER)[40], since OER, a four-electron transfer reaction, is much more sluggish than HER, a two-electron transfer reaction. Third, the current density delivered by the AEMWE correlates well with the value of R_2 - the higher R_2, the lower current density. This phenomenon reflects the fact that OER is the bottleneck process in AEMWE operations.

The best performing quinary catalysts based AEMWE was further characterized for its operation stability. Figure 5B (in terms of $\Delta V/V_0$) and Supplementary Figure 17 (in terms of V) show the remarkable operation stability of the FCNCuMO$_X$@CNT@NM//FCNCuM@CNT@CP couple based AEMWE operated under a high current density of 500 mA cm^{-2} for 100 h, with negligible decay of 0.014% in applied cell voltages. After the stability test, physical characterizations of the catalysts, including scanning electron microscopy (SEM, Supplementary Figure 18) and transmission electron microscopy (TEM, Supplementary Figure 19), were

conducted to confirm that the catalysts maintained their morphological and crystalline structures, demonstrating outstanding electrochemical and mechanical stability. The present developed high entropy catalysts, FCNCuMO$_X$@CNT and FCNCuM@CNT, are thus proven excellent electrode catalysts for AEMWEs. Supplementary Table 5 compares the electrochemical performances of the present high entropy catalysts with those of the state-of-the-art non-precious metal based catalysts reported in recent years for AEMWEs. Evidently, the FCNCuMO$_X$@CNT and FCNCuM@CNT-based AEMWE stands out among them. Particularly, in terms of the specific activity, defined as the current density achieved at 2 V per unit of combined mass loading of the anode and cathode catalysts, the FCNCuMO$_X$@CNT and FCNCuM@CNT-based AEMWE largely outperforms all other samples with an ultrahigh specific activity of 293 mA mg^{-1}, making them highly efficient catalysts for AEMWEs.

DFT study

To explore the roles and significances of constituent elements of the catalysts during HER and to understand the key factors influencing the catalytic performances of the samples, DFT calculations were conducted to investigate the synergistic effects of multiple metal active sites in alkaline HER. Hydrogen adsorption energy, ΔG_{H^*}, has been a popular descriptor for HER activities. Theoretically, a value of ΔG_{H^*} close to 0 indicates that the active site binds with H neither too strongly nor too weakly, facilitating the HER[41,42]. Nevertheless, this concept may be applicable only to HER in acidic media where hydrogen ions are abundant[43]. For HER in alkaline media, the hydrogen ions in the electrolyte need to be provided by cleavage of water molecules. Consequently, ΔG_{H^*} alone is insufficient to correlate with activities in alkaline HER. Figure 6A summarizes experimentally determined η_{10}'s achieved by the FCNCuM HEA catalyst and corresponding five quaternary alloy catalysts. Evidently, FCNCuM exhibits the highest HER activity, with the lowest overpotential of 38 mV. Nevertheless, the ΔG_{H^*} of FCNCuM (yellow line) is not the one closest to zero [Figure 6B], inconsistent with the experimental finding if ΔG_{H^*} is taken as the sole HER descriptor. Interestingly, the FCNCu quaternary alloy (Mo-absent, purple line) possesses a ΔG_{H^*} closest to zero among the six alloy samples, but exhibits the highest overpotential [Figure 6A]. With the above observations, we speculate that in alkaline HER, in addition to ΔG_{H^*}, consideration of the activation energy of the water dissociation reaction is also necessary. This speculation also aligns with the experimental finding for Tafel slopes determined for the six alloy catalysts. As evident from Supplementary Figure 13B, the Tafel slopes of the six alloy catalysts are either between 40 and 120 mV dec^{-1} (FCNCuM and FCNM) or at around 120 mV dec^{-1} (CNCuM, FNCuM, FCCuM, and FCNCu), indicating comparable Volmer and Heyrovsky steps or a single RDS of Volmer, respectively. In alkaline media, both Volmer ($H_2O + e^- \rightarrow H^* + OH^-$) and Heyrovsky ($H_2O + H^* + e^- \rightarrow H_2 + OH^-$) steps involve water dissociation, emphasizing the importance of water dissociation and also supporting the speculation.

Calculations for activation energies of water dissociation were performed for three representative models, including coupling of a strong H adsorption site with a strong OH adsorption site (H_{strong}+OH_{strong}), a strong H adsorption site with a weak OH adsorption site (H_{strong}+OH_{weak}), and a weak H adsorption site with a weak OH adsorption site (H_{weak}+OH_{weak}). ΔG_{H^*} and ΔG_{OH^*} on all possible sites, including on-top, bridge, and hollow, were first calculated for choices of the H_{strong}, H_{weak}, OH_{strong}, and OH_{weak} sites. Supplementary Table 6 summarizes some representative strong and weak sites for H and OH. The strongest and weakest adsorption sites, including FeFeFe hollow site as the H_{strong} site, FeCuCu hollow site as the H_{weak} site, Mo on-top site as the OH_{strong} site, and FeCoNi hollow site as the OH_{weak} site, were chosen to construct the three models. As evident from Figure 6C, the H_{strong}+OH_{strong} case gives the lowest activation energy (0.71 eV) required for water dissociation, which is most favorable for breaking the bond between H and OH in water molecules. The pairing of adsorption sites of H and OH and resulting activation energies for water dissociation of the three models are summarized in Supplementary Table 7 for comparison. Figure 6D and Supplementary Figure 20 illustrate the transition along the reaction path for the model of FCNCuM HEA

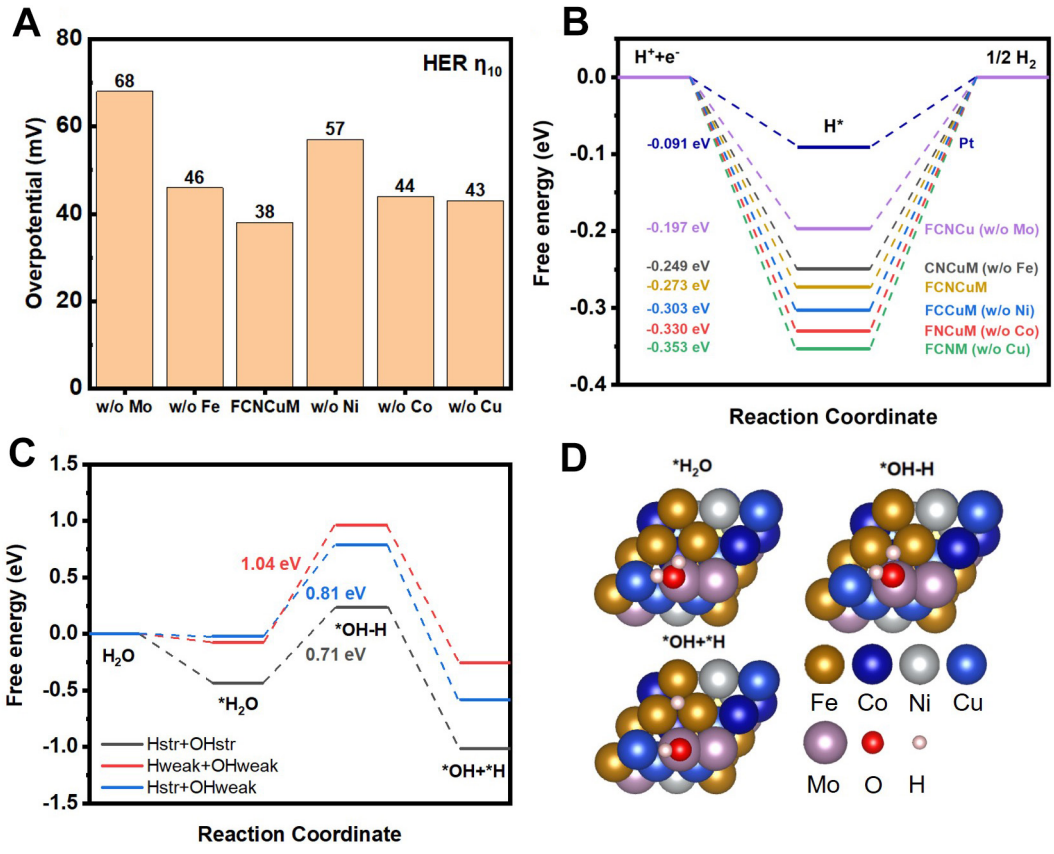

Figure 6. (A) Summary of η_{10}'s of six alloy samples; (B) ΔG_{H^*} for six alloy samples and Pt; (C) Activation energies of three representative adsorption models; (D) Illustration of transition along reaction path for FCNCuM during water dissociation.

during the water dissociation process. A water molecule is first adsorbed at the on-top site of Mo, a strong OH adsorption site. The dissociation of the water molecule proceeds, with the liberated H settling to a neighboring FeFeFe hollow site, a strong H adsorption site. It is worth mentioning that the case of H_{weak}+OH_{strong} is absent from the discussion because of the unique nature of HEAs. HEAs consist of five or more randomly distributed metal elements in the lattice, meaning that different adsorption sites are randomly dispersed on the catalyst surface. During the simulation, it was observed that H tends to be attracted to strong hydrogen adsorption sites located in the neighborhood of the strong OH adsorption site in the dissociation process, making it unlikely to have H converge to weak hydrogen adsorption sites. Consequently, this scenario is unlikely to occur in our HEA systems.

Supplementary Figure 21 summarizes the relative adsorption ability of the five constituent elements of FCNCuM toward H and OH, from which some conclusions can be drawn. First, Fe is an element with a strong hydrogen adsorption. It can assist in water dissociation but has difficulty desorbing hydrogen, which is unfavorable for HER. Second, Cu is an element with a very weak hydrogen adsorption ability. Although Cu can easily desorb hydrogen, it may cause an excessively high activation energy for water dissociation, making water cleavage and thus hydrogen ion production difficult, thus hindering HER. Third, Mo has a strong hydroxide adsorption ability, which can help lower the activation energy for water dissociation, making water cleavage and thus hydrogen ion production easier, thereby driving HER. Fourth, Co and Ni are elements with moderate hydrogen adsorption abilities. As evident from Figure 6B, the ΔG_{H^*} of the Ni-absent sample, FCCuM, is more positive as compared to that of the Co-absent sample, FNCuM,

indicating that FCCuM (w/o Ni) has a weaker hydrogen adsorption ability. This suggests that Ni has a stronger hydrogen adsorption ability as compared to that of Co. Therefore, Ni is more effective than Co in assisting cleavage of the O-H bond. Furthermore, the hydrogen adsorption ability of Ni is weaker than Fe, making dehydrogenation relatively easier, which is favorable for HER. In summary, the results indicate that Mo can stabilize OH^-, aiding bond cleavage, and Ni has a moderate hydrogen adsorption ability, which helps in bond cleavage without making desorption too difficult. Therefore, Mo and Ni are the two critical elements for catalysis of HER in alkaline media. The synergy between them ensures high HER activities. This is consistent with the experimental finding obtained in this work for alkaline HER, where FCNCu (w/o Mo) and FCCuM (w/o Ni) exhibit the poorest HER performance. It also explains why NiMo alloys are in general excellent HER catalysts[44].

CONCLUSION

A simple and fast microwave synthesis method was developed to prepare HEOs ($FCNCuMO_X$@CNT) and HEAs (FCNCuM@CNT), which exhibited outstanding catalytic efficiency toward OER and HER, respectively, in alkaline media, attributable to the cocktail effect of high entropy materials, manifested as synergistic interactions between atomically well mixed constituent elements. A highly efficient and durable AEMWE was fabricated, through teaming up the $FCNCuMO_X$@CNT anode catalyst with FCNCuM@CNT cathode catalyst, exhibiting an ultrahigh specific activity of 293 mA mg^{-1} and an outstanding operation stability of negligible decay of 0.014% after a 100 h operation under a high current density of 500 mA cm^{-2}. The success of $FCNCuMO_X$ toward catalysis of OER was found to root in the atomic scale synergy between Fe, Co, and Ni, the three main active centers of $FCNCuMO_X$. As for the HER, the atomic scale synergy between the two main active sites, Ni and Mo, of FCNCuM ensures its high catalytic efficiency. The coupling of the strong OH adsorption ability of Mo and the balanced hydrogen adsorption/desorption ability of Ni, leads to the high HER activity of FCNCuM. The present development demonstrates the unique advantages of high entropy materials as catalysts for water electrolysis. More advancements can be achieved through rational design of the high entropy materials based catalysts through composition and nanostructure engineering.

DECLARATIONS

Authors' contributions

Data curation, formal analysis, investigation, methodology, software, validation, writing - original draft: Chang, C. W.

Data curation, formal analysis, investigation: Ting, Y. C.; Yen, F. Y.; Li, G. R.

Funding acquisition, software, supervision, writing - review and editing: Lin, K. H.

Conceptualization, funding acquisition, project administration, supervision, validation, visualization, writing - review and editing: Lu, S. Y.

Availability of data and materials

Some results of supporting the study are presented in the Supplementary Materials. Other raw data that support the findings of this study are available from the corresponding author upon reasonable request.

Financial support and sponsorship

This work is financially supported by the National Science and Technology Council (NSTC) of Taiwan, under grants NSTC 112-2218-E-007-021 (SYL), NSTC 112-2628-E-007-015-(KHL), NSTC 113-2628-E-007-005- (KHL), NSTC 111-2222-E-007-004-MY2(KHL), and National Tsing Hua University (113Q2715E1, KHL). The authors greatly appreciate the beamtime of TLS 17C1 and TPS 44A1 provided by the National Synchrotron Radiation Research Center (NSRRC) of Taiwan. The authors also sincerely acknowledge the use of spherical-aberration corrected field emission TEM (JEM-ARM200FTH, JEOL Ltd.) and HRXPS (PHI

QuanteraII, ULlVAC-PHI Inc.) facilities belonging to the Instrument Center of the National Tsing Hua University of Taiwan. The authors also thank the National Center for High-performance Computing (NCHC) for providing computational and storage resources.

Conflicts of interest

All authors declared that there are no conflicts of interest.

Ethical approval and consent to participate

Not applicable.

Consent for publication

Not applicable.

Copyright

REFERENCES

1. Li, C.; Baek, J. The promise of hydrogen production from alkaline anion exchange membrane electrolyzers. *Nano. Energy.* **2021**, *87*, 106162. DOI
2. Park, Y. S.; Jang, M. J.; Jeong, J.; et al. Hierarchical chestnut-burr like structure of copper cobalt oxide electrocatalyst directly grown on Ni foam for anion exchange membrane water electrolysis. *ACS. Sustainable. Chem. Eng.* **2020**, *8*, 2344-9. DOI
3. Campagna, Z. S.; Faro, M. L.; Carbone, A.; et al. Performance and stability of a critical raw materials-free anion exchange membrane electrolysis cell. *Electrochim. Acta.* **2022**, *413*, 140078. DOI
4. Zhang, L.; Fan, Q.; Li, K.; Zhang, S.; Ma, X. First-row transition metal oxide oxygen evolution electrocatalysts: regulation strategies and mechanistic understandings. *Sustain. Energy. Fuels.* **2020**, *4*, 5417-32. DOI
5. Li, T.; Yao, Y.; Ko, B. H.; et al. Carbon-supported high-entropy oxide nanoparticles as stable electrocatalysts for oxygen reduction reactions. *Adv. Funct. Mater.* **2021**, *31*, 2010561. DOI
6. Kumar, A.; Singh, A.; Suhane, A. Mechanically alloyed high entropy alloys: existing challenges and opportunities. *J. Mater. Res. Technol.* **2022**, *17*, 2431-56. DOI
7. Wang, J.; Zhang, J.; Yu, H.; Chen, L.; Jiang, H.; Li, C. Strain engineering of high-entropy oxides enriches highly active lattice oxygen for electrocatalytic water oxidation. *ACS. Mater. Lett.* **2024**, *6*, 1739-45. DOI
8. Yao, R.; Zhou, Y.; Shi, H.; et al. Nanoporous surface high-entropy alloys as highly efficient multisite electrocatalysts for nonacidic hydrogen evolution reaction. *Adv. Funct. Mater.* **2021**, *31*, 2009613. DOI
9. Wang, Q.; Xie, J.; Qin, Y.; et al. Recent progress in high-entropy alloy electrocatalysts for hydrogen evolution reaction. *Adv. Mater. Inter.* **2024**, *11*, 2301020. DOI
10. Hooch, A. W.; Lee, S.; Lee, H. S.; et al. High-valence metal-driven electronic modulation for boosting oxygen evolution reaction in high-entropy spinel oxide. *Adv. Funct. Mater.* **2024**, *34*, 2309438. DOI
11. Kresse, G.; Furthmüller, J. Efficiency of ab-initio total energy calculations for metals and semiconductors using a plane-wave basis set. *Comput. Mater. Sci.* **1996**, *6*, 15-50. DOI
12. Kresse, G.; Furthmüller, J. Efficient iterative schemes for *ab initio* total-energy calculations using a plane-wave basis set. *Phys. Rev. B.* **1996**, *54*, 11169. DOI
13. Kresse, G.; Joubert, D. From ultrasoft pseudopotentials to the projector augmented-wave method. *Phys. Rev. B.* **1999**, *59*, 1758. DOI
14. Blöchl, P. E. Projector augmented-wave method. *Phys. Rev. B.* **1994**, *50*, 17953. DOI
15. Perdew, J. P.; Burke, K.; Ernzerhof, M. Generalized gradient approximation made simple. *Phys. Rev. Lett.* **1996**, *77*, 3865-8. DOI PubMed
16. Zhang, B.; Wang, J.; Liu, J.; et al. Dual-descriptor tailoring: the hydroxyl adsorption energy-dependent hydrogen evolution kinetics of high-valance state doped Ni_3N in alkaline media. *ACS. Catal.* **2019**, *9*, 9332-8. DOI
17. Henkelman, G.; Uberuaga, B. P.; Jónsson, H. A climbing image nudged elastic band method for finding saddle points and minimum energy paths. *J. Chem. Phys.* **2000**, *113*, 9901-4. DOI
18. Martín-garcía, L.; Bernal-villamil, I.; Oujja, M.; et al. Unconventional properties of nanometric FeO(111) films on Ru(0001): stoichiometry and surface structure. *J. Mater. Chem. C.* **2016**, *4*, 1850-9. DOI
19. Sankaranarayanan, R.; Shailajha, S.; Mubina, M. S. K.; Anilkumar, C. P. Effect of Ni^{2+} and Fe^{3+} ion concentrations on structural, optical, magnetic, and impedance response of $NiFe_2O_4$ nanoparticles prepared by sol-gel process. *J. Supercond. Nov. Magn.* **2020**, *33*, 3631-42. DOI
20. Song, X. Z.; Zhao, Y. H.; Zhang, F.; et al. Coupling plant polyphenol coordination assembly with $Co(OH)_2$ to enhance electrocatalytic

performance towards oxygen evolution reaction. *Nanomaterials* **2022**, *12*, 3972. DOI PubMed PMC

21. Biesinger, M. C.; Payne, B. P.; Grosvenor, A. P.; Lau, L. W.; Gerson, A. R.; Smart, R. S. Resolving surface chemical states in XPS analysis of first row transition metals, oxides and hydroxides: Cr, Mn, Fe, Co and Ni. *Appl. Surf. Sci.* **2011**, *257*, 2717-30. DOI
22. Weidler, N.; Schuch, J.; Knaus, F.; et al. X-ray Photoelectron spectroscopic investigation of plasma-enhanced chemical vapor deposited NiO_x , $NiO_x(OH)_y$, and $CoNiO_x(OH)_y$: influence of the chemical composition on the catalytic activity for the oxygen evolution reaction. *J. Phys. Chem. C.* **2017**, *121*, 6455-63. DOI
23. Sivkov, D. V.; Petrova, O. V.; Nekipelov, S. V.; et al. The Identification of Cu-O-C bond in Cu/MWCNTs hybrid nanocomposite by XPS and NEXAFS spectroscopy. *Nanomaterials* **2021**, *11*, 2993. DOI
24. Wang, Z.; Zhang, G.; Fan, X.; Jin, J.; Zhang, L.; Du, Y. Corrosion behavior and surface characterization of an equiatomic CoCrFeMoNi high-entropy alloy under various pH conditions. *J. Alloys. Compd.* **2022**, *900*, 163432. DOI
25. Gomez-Iriarte, G. A.; Pentón-Madrigal, A.; de, O. L. A. S.; Sinnecker, J. P. XPS study in $BiFeO_3$ surface modified by argon etching. *Materials* **2022**, *15*, 4285. DOI PubMed PMC
26. Wang, T.; Jiang, Z.; Chu, K. H.; et al. X-Shaped α-FeOOH with enhanced charge separation for visible-light-driven photocatalytic overall water splitting. *ChemSusChem* **2018**, *11*, 1365-73. DOI
27. O'donnell, S.; O'neill, D.; Shiel, K.; et al. Plasma-enhanced atomic layer deposition of nickel and nickel oxide on silicon for photoelectrochemical applications. *J. Phys. D:. Appl. Phys.* **2023**, *56*, 415302. DOI
28. Xu, S.; Sheng, R.; Cao, Y.; Yan, J. Reversibly switching water droplets wettability on hierarchical structured Cu_2S mesh for efficient oil/water separation. *Sci. Rep.* **2019**, *9*, 12486. DOI PubMed PMC
29. Liu, J.; Tang, S.; Lu, Y.; et al. Synthesis of Mo_2N nanolayer coated MoO_2 hollow nanostructures as high-performance anode materials for lithium-ion batteries. *Energy. Environ. Sci.* **2013**, *6*, 2691. DOI
30. Cheng, B.; Lou, H.; Sarkar, A.; et al. Lattice distortion and stability of $(Co_{0.2}Cu_{0.2}Mg_{0.2}Ni_{0.2}Zn_{0.2})O$ high-entropy oxide under high pressure. *Mater. Today. Adv.* **2020**, *8*, 100102. DOI
31. Diallo, A.; Beye, A.; Doyle, T.; Park, E.; Maaza, M. Green synthesis of Co_3O_4 nanoparticles via *aspalathus linearis* : physical properties. *Green. Chem. Lett. Rev.* **2015**, *8*, 30-6. DOI
32. Wang, D.; Liu, Z.; Du, S.; et al. Low-temperature synthesis of small-sized high-entropy oxides for water oxidation. *J. Mater. Chem. A.* **2019**, *7*, 24211-6. DOI
33. Masikhwa, T. M.; Madito, M. J.; Momodu, D.; Bello, A.; Dangbegnon, J. K.; Manyala, N. High electrochemical performance of hybrid cobalt oxyhydroxide/nickel foam graphene. *J. Colloid. Interface. Sci.* **2016**, *484*, 77-85. DOI PubMed
34. Lin, Z.; Bu, P.; Xiao, Y.; Gao, Q.; Diao, P. β- and γ-NiFeOOH electrocatalysts for an efficient oxygen evolution reaction: an electrochemical activation energy aspect. *J. Mater. Chem. A.* **2022**, *10*, 20847-55. DOI
35. Zhang, J.; Wang, T.; Liu, P.; et al. Efficient hydrogen production on $MoNi_4$ electrocatalysts with fast water dissociation kinetics. *Nat. Commun.* **2017**, *8*, 15437. DOI PubMed PMC
36. He, L.; Cheng, P.; Cheng, C.; Huang, C.; Hsieh, C.; Lu, S. $(Ni_xFe_yCo_{6-x-y})Mo_6C$ cuboids as outstanding bifunctional electrocatalysts for overall water splitting. *Appl. Catal. B:Environ.* **2021**, *290*, 120049. DOI
37. Suen, N. T.; Hung, S. F.; Quan, Q.; Zhang, N.; Xu, Y. J.; Chen, H. M. Electrocatalysis for the oxygen evolution reaction: recent development and future perspectives. *Chem. Soc. Rev.* **2017**, *46*, 337-65. DOI PubMed
38. Friebel, D.; Louie, M. W.; Bajdich, M.; et al. Identification of highly active Fe sites in (Ni,Fe)OOH for electrocatalytic water splitting. *J. Am. Chem. Soc.* **2015**, *137*, 1305-13. DOI
39. González-flores, D.; Klingan, K.; Chernev, P.; et al. Nickel-iron catalysts for electrochemical water oxidation - redox synergism investigated by *in situ* X-ray spectroscopy with millisecond time resolution. *Sustain. Energy. Fuels.* **2018**, *2*, 1986-94. DOI
40. Xu, Q.; Zhang, L.; Zhang, J.; et al. Anion exchange membrane water electrolyzer: electrode design, lab-scaled testing system and performance evaluation. *EnergyChem* **2022**, *4*, 100087. DOI
41. Ullah, F.; Ayub, K.; Mahmood, T. High performance SACs for HER process using late first-row transition metals anchored on graphyne support: a DFT insight. *Int. J. Hydrogen. Energy.* **2021**, *46*, 37814-23. DOI
42. Zhao, X.; Zhang, Z.; Cao, X.; et al. Elucidating the sources of activity and stability of FeP electrocatalyst for hydrogen evolution reactions in acidic and alkaline media. *Appl. Catal. B:Environ.* **2020**, *260*, 118156. DOI
43. Danilovic, N.; Subbaraman, R.; Strmcnik, D.; Stamenkovic, V.; Markovic, N. Electrocatalysis of the HER in acid and alkaline media. *J. Serb. Chem. Soc.* **2013**, *78*, 2007-15. DOI
44. Raja, D.; Cheng, C. C.; Ting, Y. C.; Lu, S. Y. NiMo-MOF-derived carbon-armored Ni_4Mo alloy of an interwoven nanosheet structure as an outstanding pH-universal catalyst for hydrogen evolution reaction at high current densities. *ACS. Appl. Mater. Interfaces.* **2023**, *15*, 20130-40. DOI